Yvonne Chen (Autor)

Meniscus Stability in Rotating Systems

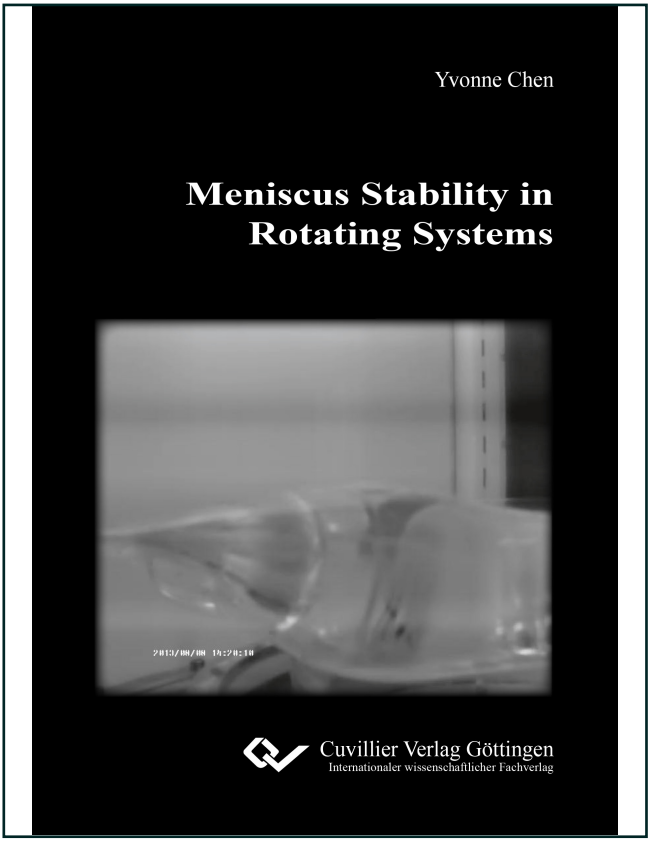

https://cuvillier.de/de/shop/publications/6989

Chapter 1

Introduction

The knowledge of behavior of liquids with free surfaces to their surrounding gaseous phase in compensated gravity is essential to the development of tank systems for spacecrafts. In microgravity, the liquid behavior is dominated by capillary forces, which are used to position and redistribute liquid propellant in a desired way for the mission. The body forces occurring due to residual accelerations, which can be caused by spin during the ballistic flight phases, force the liquid to reorient towards a new equilibrium state of the free surface. Due to spin the liquid is driven away from the tank outlet and located along tank walls in partially filled tanks. To assure enough liquid fuel over the tank outlet, so-called Propellant Management Devices (PMD's), are employed. A PMD is a static, usually metal structure, which either provides a passage way for a liquid in microgravity or stores a certain amount of liquid at a desired location. Some PMD's are designed to be refillable in periods of microgravity due to openings in the outer housing or by a housing composed of perforated metallic sheets. These reservoirs are refilled in periods of compensated gravity in order to provide the required amount of liquid fuel for attitude control or other maneuverings. Relatively large disturbances, such as lateral accelerations and spin, can drive the liquid fuel out of the reservoir, resulting in malfunction of the device. During spilling, gas enters the device such that only a residual amount of liquid propellant can be kept in the reservoir. Moreover, the connection to the bulk liquid in the tank may be interrupted such that refilling of the reservoir is disrupted. Hence, a PMD with two parallel disks forming the inlet and a venting tube at the topmost point of the outer housing shall be designed such that its refillable structure is only filled with liquid without any gas or vapor being easily trapped during operations.

Goal of this work is to understand the liquid free surfaces behavior influenced by centrifugal accelerations in microgravity. For the analyses, a generic model of a refillable reservoir is used consisting of two coaxial circular disks, either without segments or segmented by vertically mounted baffles being distributed evenly along the disk perimeter. A tube is assembled at the center of the upper disk representing the venting tube of the PMD. The intention is to

determine the angular speeds at which initially stable menisci fail to sustain. Here, four cases are investigated: for relatively large angular speeds, the initially convex meniscus between the disks bulges outwards to the point, when the capillary forces cannot balance the centrifugal forces, and the liquid spills out of the space between the disks. This case is called supercritical. The second case is for large radii of the central tube and small separation of the disks, the meniscus in the central tube becomes unstable before instability of the free surfaces between the disks occurs. For the third case, if the angular speed is negligible, for a certain combination of geometrical parameters, capillary rise occurs in the tube, and the liquid between the disks moves towards the center of the model. A fourth case is for an appropriate choice of geometrical parameters and small rotation: equilibrium of the free surfaces in the tube and between the disks establishes.

In the first part of this study, the profiles of the menisci between the disks and in the tube in equilibrium and the stability limit of the free surfaces in the rotating models are computed for varied geometrical parameters. For this purpose, sets of differential equations describing the pressure balance are solved by means of the Adams-Bashforth method to determine the meniscus profiles. Solving an additional equation including the perturbation gives the stability limit due to maximum curvature of these menisci. Computing the profiles, the corresponding boundary conditions are taken into account for the meniscus in the central tube and the free surface between the disks, respectively. For the free surface between the disks, the pressure difference across the interface in the central tube at its axis of rotation is implemented in the related set of equations determining its shape and stability. Moreover, free surfaces in equilibrium without rotation are computed. For this case, the aspect ratios of the tube radius and the distance between the disks are determined, for which no capillary rise occurs in the central tube yet.

However, analytical solutions for the shape and the stability limit of the free surfaces can only be obtained for the unsegmented models. For segmented models, analytical solutions are difficult due to the three-dimensional nature of the curved surfaces at the outer rims of the circular disks. Hence, shapes and stability are studied with the numerical program *Surface Evolver* by Brakke [13]. This tool only provides statical solutions for the meniscus shapes under user-defined constraints, i.e., all dynamical effects, e.g., occurring during reorientation from a change of longitudinal acceleration, are neglected. The graphical user interface SE-FIT [22] allows an efficient study of a wide range of parameters using the routine *Parameter Sweep Function* (PSF). PSF allows an automatic change of selected parameters such as angular speed and radii.

This first study only provides information about the free surfaces in equilibrium by solving the pressure balance with related constraints: static contact angle, a moving contact line at the tube wall and a fixed contact line at the outer edges of the disks. These results are

compared to experimental data, for which so far neglected dynamical effects, i.e., friction, inertia and damping behavior, play an important role. To include dynamical effects, the CFD tool *OpenFOAM*® is used to study the liquid behavior in the rotating models. The goal of this part is the determination of the free surface stability in selected models considering dynamical effects. The angular speed is kept constant for each computation to allow comparison to the results of the statical numerical analyses, for which solid-body rotation is valid. From the simulations, pressure fields and velocity distributions are computed for angular speeds resulting in stable configurations of the free surfaces or unstable ones. Hence, regions of maximum and minimum velocities and pressures are determined with respect to sub-critical and supercritical cases.

The results of the previous analyses are compared to those of drop tower experiments. With the assumption of solid-body rotation, the rotation was established some time before the free fall. At a constant angular speed in each test, either oscillatory movements of the free surfaces around constant locations or instability of the free surfaces, when the meniscus, initially being in the central tube, moved into the space between the disks, was observed. Additionally, because of the limited number of tests, the critical angular speed related to maximum curvatures could not be identified. For comparison, the sets of parameters investigated in the experiments are studied with OpenFOAM®. In contrast to the experiments, the duration of the simulation was extended to observe the damping behavior of the liquid before reaching equilibrium or instability of the free surface movement.

This work is divided as follows. In Chap. 2, the theoretical background is described for understanding the behavior of free surfaces in rotating systems. It is followed by an overview of the literature which contains analytical and experimental studies about the shape and stability of menisci in rotating systems. Moreover, free surfaces with constant mean curvature relevant for the models without rotation are introduced. A short overview of the possible application of the PMD is given. The goal of this work is deducted from the theoretical background. The relevant mathematical formulations for determining shape and stability of the free surfaces under rotation in the unsegmented models are given in Chap. 3. The scaling of the relevant parameters and equations is shown. Additionally, the limiting cases are investigated: for the unsegmented models without rotation, the geometrical aspect ratios of the central tube radius and the distance between the parallel disks are determined for which no capillary rise occurs in the central tube. The shape of the corresponding menisci between the disks are computed. Additionally, the critical values of the rotational Bond numbers, related to the angular speeds, are determined giving the stability limit of the free surfaces in the unsegmented models. A criterion is derived to distinguish if the meniscus either in the central tube or between the disks becomes unstable for a supercritical Bond numbers. After an introduction of the Surface Evolver, an overview of the applications of this numerical program is provided in Chap. 4. A

benchmark case and the numerical models are described, before presenting the results of the computations. Cases with stable equilibrium menisci are given for segmented and unsegmented models. The critical values of the rotational Bond numbers for a wide range of geometrical parameters are shown. Dyson's inequality condition [42] is taken into account to show the dependence of the stability limit of the free surface between the disks on the static contact angle. Additionally, solutions for the meniscus profiles in the tube and between the disks are given for the limiting cases without rotation and compared to those of the numerical integration. Chap. 5 gives a brief overview of applications of the relevant OpenFOAM® solver. The modification of this solver is introduced providing stability of numerical schemes. Results for different model configurations for sub- and supercritical Bond numbers are presented. In Chap. 6, the setup and settings of the free fall tests are described. The settling times of the free surfaces and other dynamical effects are determined in experiments performed without rotation. The results of all the analyses and the experiments are compared in Chap. 7. After a summary of this work in Chap. 8, a possible application of the tested models with related free fall experiments of the application is provided in Chap. 9.

Chapter 2

Theoretical Background and State of the Art

2.1 Rotation

Three types of rotating bodies can be distinguished. The simplest one is a body rotating around its axis with a constant angular speed and being in the state of solid-body rotation, for which the Coriolis force can be neglected. In the second case, this body is additionally in movement with a constant velocity. A third case occurs when there is angular speed only which does not change with time. The general form of the acceleration for a rigid body in rotation writes according to White [122]

$$\mathbf{a} = \underbrace{\frac{\mathrm{d}\mathbf{v}}{\mathrm{d}t}}_{\text{translational motion}} + \underbrace{\frac{\mathrm{d}\boldsymbol{\Omega}}{\mathrm{d}t} \times \mathbf{R}}_{\text{temporal change of the rotation}} + \underbrace{\boldsymbol{\Omega} \times (\boldsymbol{\Omega} \times \mathbf{R})}_{\text{centripetal acceleration}} . \tag{2.1}$$

The velocity in the translational motion is

$$\mathbf{v} = \mathbf{v}_0 + \boldsymbol{\Omega} \times \mathbf{R} , \tag{2.2}$$

where $\mathbf{v}_0$ is the velocity at the center of mass of the rigid body, $\mathbf{R}$ corresponds to the vector from the initial location of the center of mass to a point P, and $\boldsymbol{\Omega}$ is the angular speed. The temporal change of the rotation characterizes the linear acceleration due to changes in $\boldsymbol{\Omega}$.

White [122] claimed that for most of fluid flows rarely all three terms are relevant. The author gave the microgravity environment as an example, in which the state of solid-body rotation can be reached in a finite amount of time. In this work, solid-body rotation is assumed for the models (see Chap. 3), and for this state Eq. 2.1 simplifies to

$$\mathbf{a} = \boldsymbol{\Omega} \times (\boldsymbol{\Omega} \times \mathbf{R}) . \tag{2.3}$$

The acceleration due to a constant angular speed can be also written as

$$a_{rot} \;=\; \dot{\varphi}^2\, R \;, \tag{2.4}$$

where $\dot{\varphi} = |\mathbf{\Omega}|$ is the angular speed and R the corresponding radius.

For a rigid body rotating around its axis, the Coriolis force writes

$$\mathbf{f}_C \;=\; -2 \iiint_V \rho(\mathbf{\Omega} \times \mathbf{v}_t)\mathrm{d}V \;, \tag{2.5}$$

where $\mathbf{v}_t$ characterizes the velocity relative to the reference system (compare Fig. 2.1). The acceleration caused by the Coriolis effect writes

$$\mathbf{a}_C \;=\; -2\,(\mathbf{\Omega} \times \mathbf{v}_t) \;. \tag{2.6}$$

It results from the change of velocity in time and the variation of the velocity with position of a point mass.

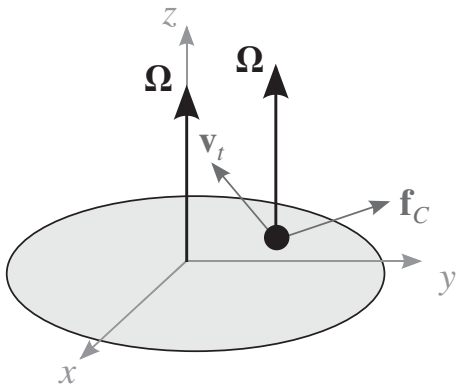

Figure 2.1: Coriolis force acting on a rotating point mass (black dot).

2.2 Surface Tension

A fluid forms an interface with another fluid, when the two are in contact with each other. In the bulk liquid, the molecules are packed close since they attract each other. At the free surface, half of the neighbors of the molecules are missing compared to the molecules in the bulk liquid. Therefore, those molecules at the interface are under tension. If the liquid is in contact with a gaseous phase, this results in an unbalanced cohesive force to the inside of the liquid [3]. A work has to be executed to bring the molecules from the inside of the liquid to the free surface. The increasing number of molecules at the interface causes an enlargement of the free surface area due to the specific work $\mathrm{d}W$. Hence, the surface tension can be described by [122]

$$\sigma \;=\; \frac{\mathrm{d}W}{\mathrm{d}A} \;=\; \frac{F\,\mathrm{d}s}{L\,\mathrm{d}s} \;=\; \frac{F}{L} \;, \tag{2.7}$$

where L is the length of the area. When isothermal conditions are assumed, $\mathrm{d}W$ equates the free surface energy E_{sur}. The coefficient of the surface tension σ can be expressed as the ratio of the free surface energy and the surface area [3]

$$\sigma \;=\; \frac{E_{sur}}{L\,\mathrm{d}s}\;. \tag{2.8}$$

The value of the coefficient σ depends on the temperature and the pressure of the fluids [86, 103]. With decreasing pressure or decreasing temperature, the value of σ increases.

For a liquid-gas-system, the curved surface provides a resulting force into the bulk liquid. The force leads to an increase of the cohesion pressure for convex-shaped free surfaces, while this force reduces the cohesion pressure for concave surfaces. The relation for the change in pressure due to curvature can be illustrated on a single fluid element $\mathrm{d}A$.

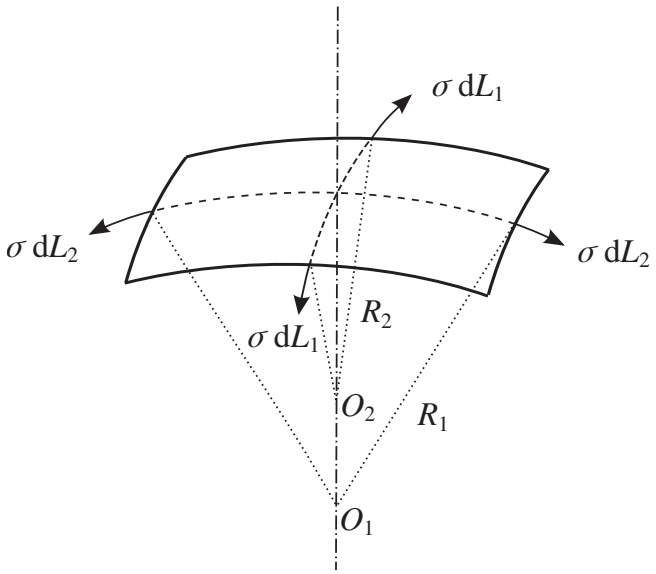

Figure 2.2: Single fluid element $\mathrm{d}A$ with the principal radii R_1 and R_2.

From the element $\mathrm{d}A$, the tangential forces F_1 and F_2 act on the vicinal elements of $\mathrm{d}A$ and provide a resulting force directed into the liquid. The forces can be expressed by

$$F_1 \;=\; 2\,\sigma \mathrm{d}L_2\,\sin(\psi) \quad \text{and} \quad F_2 \;=\; 2\,\sigma \mathrm{d}L_1\,\sin(\psi)\;. \tag{2.9}$$

The angle $\psi << 1$ can be assumed. Therefore, $\sin(\psi) \approx \psi$ such that ψ writes

$$\psi \;=\; \frac{\mathrm{d}L_1}{2\,R_1} \;=\; \frac{\mathrm{d}L_2}{2\,R_2}\;, \tag{2.10}$$

which results in $\frac{1}{2}\mathrm{d}L_i \;=\; \psi\,R_i$. Hence, the forces F_i can be written as

$$F_1 \;=\; \sigma\frac{\mathrm{d}A}{R_1} \quad \text{and} \quad F_2 \;=\; \sigma\frac{\mathrm{d}A}{R_2}\;, \tag{2.11}$$

where $\mathrm{d}A = \mathrm{d}L_1\,\mathrm{d}L_2$. Dividing Eq. 2.11 by the element area $\mathrm{d}A$, the pressure difference at the liquid surface is determined by the Young-Laplace equation [1]

$$\Delta p = \sigma \left(\frac{1}{R_1} + \frac{1}{R_2} \right) , \tag{2.12}$$

where R_i are the principal radii. For convex surfaces, e.g., a droplet, the pressure in the liquid exceeds that of the gaseous phase. The curvature is positive. Consequently, a negative curvature is for concave surfaces.

2.3 Contact Angle

When a liquid, being in contact with a second fluid, interacts with a solid surface, the contact angle θ is formed between the contact line of the two fluids meeting the solid surface. In this respect, the second fluid can be either a gas, a vapor, or another liquid. The value of θ is measured by the tangent of fluid 1 to either the interface of another fluid and a solid (see Fig. 2.3 (a)) or to the interface of two fluids, e.g., another liquid and a gas, at the contact line (see Fig. 2.3 (b)). Some authors [51, 113, 114, 118] claimed the existence of a micro-zone with a very thin film at the wall instead of a contact point, where all three phases coincide. The micro-zone is not of main interest in the macroscopic case and will not be considered further. Instead, the model of a contact line is used to explain some parameters in the following. The contact angle is a function of all three materials at this contact line and not a property of fluid 1 and fluid 2.

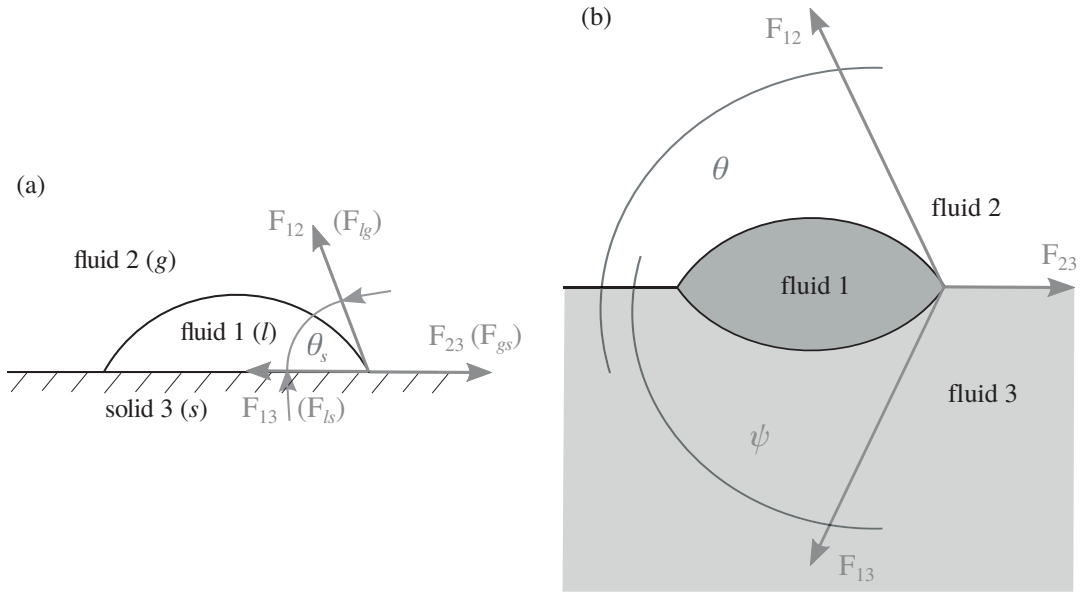

Figure 2.3: Contact angle between (a) two fluids and a solid surface and (b) between three fluids.

The contact angle can be classified into three different types according to Duquennoy et al. [40] and Kistler [61]. The real contact angle θ_{real} appears a few molecule layers away from the solid wall, i.e., 3 to 30 nm. Hence, no continuum mechanics determine its behavior. The relevant forces and their fluctuations act at relatively small distances between the molecules. The free surface cannot be regarded as a sharp interface in the molecule layers, it is rather a surface with a continuous exchange of molecules between the fluids. Due to thermal motion, a few molecules always enter the other fluid [69]. In a distance of 0.1 μm or closer to the solid wall, the microscopic contact angle θ_{mic} is present. In this region, the density difference between the gaseous and the liquid phase has a discontinuous change and the surface tension σ is defined. The measurable contact angle is also known as the apparent contact angle θ_{app}. It is located at a distance of 1 to 10 μm from the solid wall. θ_{app} differs from the thermodynamic equilibrium, since the slope of the free surface below the resolution for the observation can be different. Each type of contact angle is further subdivided into a static and a dynamic contact angle.

2.3.1 Static Contact Angle

The static contact angle θ_s appears for contact lines remaining still on solid surfaces. The value of θ_s is related to the relative magnitudes of the microscopic adhesive and cohesive forces [37].

For the case of two fluids interacting with a solid surface (see Fig. 2.3 (a)), the solid is able to compensate the forces normal to its surface. Hence, only the forces tangential to the solid surface must balance each other. The equilibrium of these stresses along the contact line is caused by the minimization of energy [69]. The balance of the forces tangential to the solid surface can be written as

$$F_{gs} \;=\; F_{lg}\cos\left(\theta_s\right) \;+\; F_{ls}\;. \tag{2.13}$$

For this force balance, the body forces, e.g., due to gravitation, are neglected. The forces in this equilibrium are

$$F_{ls} \;=\; \sigma_{ls}\mathrm{d}L_1, \quad F_{gs} \;=\; \sigma_{gs}\mathrm{d}L_1, \quad \text{and} \quad F_{lg} \;=\; \sigma_{lg}\mathrm{d}L_1\;. \tag{2.14}$$

Combining Eqs. 2.13 and 2.14 yields

$$\cos\left(\theta_s\right) \;=\; \frac{\sigma_{gs} \;-\; \sigma_{ls}}{\sigma_{lg}}\;. \tag{2.15}$$

This is also known as Young's equation [3] or Young-Dupré equation as it was first derived by Young [123]. In case of the three fluid phases (Fig. 2.3 (b)), Neumann's boundary condition is given by [122]

$$\sigma_{12} \;+\; \sigma_{23} \;+\; \sigma_{31} \;=\; 0\;, \tag{2.16}$$

and the equilibrium of forces at the contact line yields

$$\sigma_{23} = \sigma_{13} \cos(\theta) + \sigma_{12} \cos(\psi) , \tag{2.17}$$

$$\sigma_{13} \sin(\theta) = \sigma_{12} \sin(\psi) . \tag{2.18}$$

For an interface in contact with a solid wall, the boundary condition results from Eq. 2.15

$$\sigma_{gs} = \sigma_{ls} + \sigma_{lg} \cos\theta_s . \tag{2.19}$$

Different phenomena can be observed for various contact angle values θ_s between fluids and solids. If $\theta_s < \pi/2$, the liquid wets the surface of the solid. With decreasing values of θ_s an increase of the liquid surface occurs. For a contact angle of $\theta_s = \pi$, the relation $\sigma_{gs} + \sigma_{ls} = \sigma_{lg}$ is valid [122]. This physical phenomenon is called non-wetting. Total or perfect wetting occurs for zero static contact angles, which is described by $\sigma_{gs} - \sigma_{ls} \geq \sigma_{lg}$ [122]. A zero static contact angle is typical for cryogenic liquids in contact with metal surfaces and, hence, this value represents θ_s in this study.

2.3.2 Dynamic Contact Angle

When the contact line moves over a solid surface, the contact angle differs from the static contact angle θ_s and is known as the dynamic contact angle θ_d. At the advancing contact line the fluid has the advancing (dynamic) contact angle θ_{da} with the solid surface, while the receding contact angle θ_{dr} is the angle between the solid surface and the fluid at the receding contact line. The process occurs in scenarios such as forced wetting, forced dewetting or spontaneous spreading [61]. The forced wetting is imposed by hydrodynamic or mechanical forces externally. The forces cause an increasing of the area between the liquid and the solid beyond the conditions of the static equilibrium. The liquid or, alternatively, the solid front is driven by a constant velocity. A stationary coating process is mentioned as an example, during which the solid body is moved relatively to the liquid. Moreover, Kistler [61] distinguished the wetting process between a complete wetting and a partial wetting. The complete wetting occurs for non-volatile liquids with a static contact angle of zero. The dynamic contact angle can be well approximated and is insensitive to specific liquid-solid interactions. The partial wetting depends also on the solid roughness which causes a contact angle hysteresis between θ_{da} and θ_{dr}: $\theta_{dr} \leq \theta_e \leq \theta_{da}$ (cf. Fig. 2.4). In this context, θ_e describes the contact angle at thermodynamic equilibrium. In the case of spontaneous spreading, the liquid moves over the solid surface unsteadily toward the thermodynamical equilibrium. Hence, the free energy is reduced with the increase of the wetted area on the solid surface. An example for this is the wetting process in porous media. In either forced wetting or spontaneous spreading, the advancing contact angle θ_{da} increases with increasing contact line speed. A higher viscosity of the liquid results in a more significant

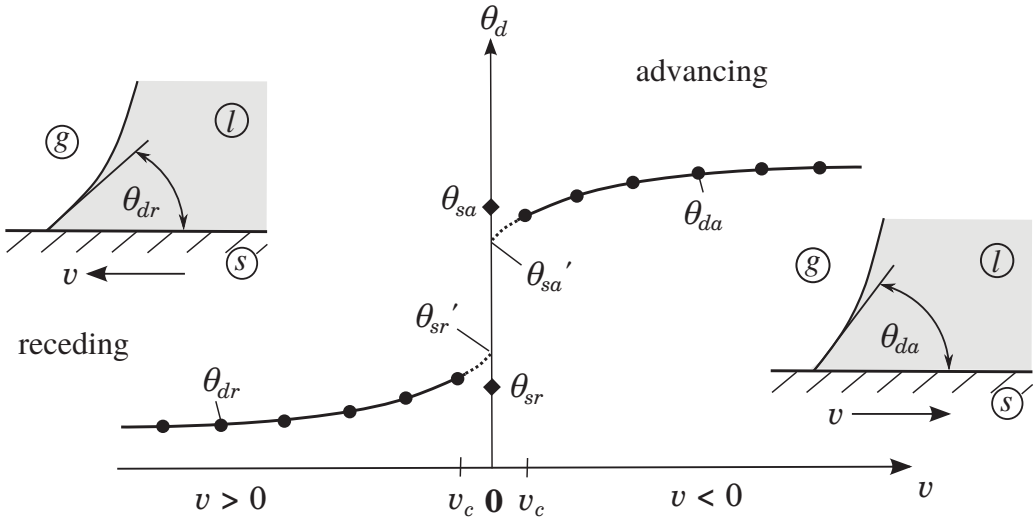

Figure 2.4: Typical behavior of the dynamic contact angle θ_d dependent on the velocity of a solid wall $\boldsymbol{v}$ according to Dussan [41]. For the case of a receding contact line, θ_d decreases when v increases in its absolute value. If $v > 0$, θ_d increases with increasing contact line speed. For $v \to 0$, the dynamic contact approaches either the static receding contact angle θ_{sr} or the static advancing contact angle θ_{sa}. The measured values ($\bullet$) for these contact angles θ_{sr}' and θ_{sa}' can differ from the extrapolated values θ_{sr} and θ_{sa}, caused by a stick-slip motion of the contact line.

increasing of θ_{da}. In the process of forced wetting, the dynamic contact angle approaches π when the contact line approaches a critical speed v_c. If the contact line speed exceeds v_c, gas bubbles can be entrapped into the liquid layer. For dewetting processes, θ_d approaches zero if v approaches v_c. In this case, θ_d decreases with increasing contact line speed.

The behavior of a moving contact line is illustrated in Fig. 2.4. At low speeds of the contact line, the dynamic contact angle approaches either the static advancing or the static receding contact angle θ_{sa} or θ_{sr}. In the lower regimes of the contact line speed, a difference between the extrapolated contact angles θ_{sr}' and θ_{sa}' and the measured static contact angles θ_{sr} and θ_{sa} occurs. This phenomenon results from a stick-slip behavior of the contact line [41, 61]. At these relatively low velocities, the contact line moves unsteadily over a rough solid surface. Due to the unsteady movement, the contact line is pinned temporarily on the solid surface. At higher contact line speeds, this phenomenon often disappears. This stick-slip behavior occurs usually for partial wetting. If the solid surface is wetted by a precursor film, the no-slip hypothesis is valid. Spontaneous wetting proceeds faster on prewetted surfaces, e.g., by a precursor film, compared to dry solid surfaces. In the case of forced wetting, the apparent contact angle is smaller on a preexisting film compared to dry surfaces. The precursor film is especially relevant in case of total wetting liquids. This film with a thickness of less than 1 μm propagates ahead of the wetting line for sufficient slow movements of the contact line [61]. It can be caused

by evaporation of liquid followed by condensation on the solid surface and structural effects between the liquid molecules and the solid molecules. For liquid-solid combination with contact angles θ_s different from zero, the precursor film is originated from imperfections of the solid surface. The imperfections act like capillary channels, into which the liquid wicks ahead of the macroscopic contact line. By means of this film, the spontaneous wetting is increased compared to dry surfaces, while the forced wetting is slowed down compared to dry surfaces [61]. If θ_{app} is much larger than zero or if contact line speeds are large, no precursor film can be established.

To summarize, the dynamic contact angle is influenced by the viscosity of the liquid, the roughness or porosity of the surface, chemical inhomogeneities, electrical charges of the solid surfaces, and impurities of the materials. Additionally, it depends on the ratios of the densities and viscosities of the fluids [61].

2.3.3 Pinned Contact Line

In this work, a moving contact line is present. Caused by the upward movement of the liquid in the tube, the contact line for the menisci between the disks moves towards the center of the model following Young's condition for the contact angle (Eq. 2.19). Regarding the stability of the free surfaces between the parallel disks in terms of rotation, the case of a pinned contact line has to be considered. In this case, the contact angle is not constant as it is assumed for the moving contact line in the tube.

The effect of edges on contact lines have been studied widely. Gibbs [47] set up two inequalities to describe the contact line stability on a solid edge for a system with two fluids 1 and 2. The static equilibrium contact angle θ_e is measured through 1, while the smooth solid surface equilibrium contact angle measured through 2 is $\pi - \theta_e$. From the Young-Dupré equation, Gibbs deduced for a contact line, which is located at the edge of a solid

$$\sigma_{lg}\cos(\theta_{ls}) \leq \sigma_{gs} - \sigma_{ls} \qquad \text{and} \tag{2.20}$$

$$\sigma_{lg}\cos(\theta_{gs}) \leq \sigma_{ls} - \sigma_{gs}\ , \tag{2.21}$$

where the angles θ_{ls} and θ_{gs} are the angles between the contact line and the solid from the liquid side and from the gas side, respectively. The notation is explained in Fig. 2.5.

Gibbs' inequalities can also be expressed by

$$\cos(\theta_{ls}) \leq \cos(\theta_e) \qquad \text{and} \tag{2.22}$$

$$\cos(\theta_{gs}) \leq -\cos(\theta_e)\ , \tag{2.23}$$

with θ_e as the static equilibrium contact angle between the solid and the liquid.

Dyson [42] claimed that these inequalities provided by Gibbs are not sufficient to describe the contact line stability at edges. He gave a counterexample with a cylindrical vessel made

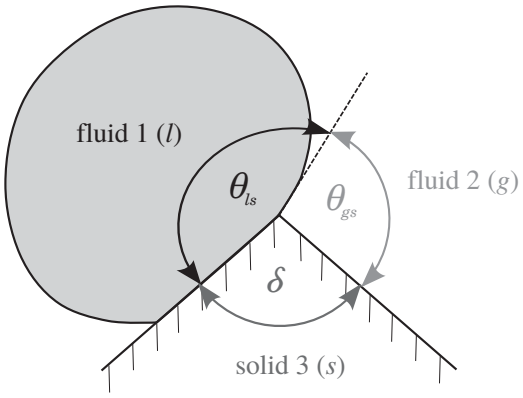

Figure 2.5: Contact line between a liquid and a gas at a solid edge for $\theta_{ls} > \pi/2$ and $\delta < \pi$.

of thin rigid material filled with liquid, which is located on the bottom of a rigid rectangular container filled with another liquid. The immiscible liquids have the same density such that no body forces act on the system. The liquid-liquid interface is assumed to be the planar disk bounded by the top edges of the cylindrical container. If the contact angles are chosen to be $\theta_{ls} = \pi/2$ and $\theta_{gs} = 3\,\pi/2$, the equilibrium static contact angle is consequently $\theta_e = \pi/3$. This system satisfies Eq. 2.22 but violates Eq. 2.23. Hence, Dyson [42] derived another criterion to describe the equilibrium condition of a contact line at an edge with an angle $\delta \leq \pi$ (see Fig. 2.5)

$$\theta_e \leq \theta_{ls} \leq (\pi - \delta) + \theta_e \,. \tag{2.24}$$

This means that a contact line with $\theta_e = 0°$ is stable at an edge of $\delta = \pi/2$ if, and only if, $\theta_{ls} \leq \pi/2$.

Fang and Amirfazli [44] analyzed the stability of a single liquid drop on a solid edge of a pillar. The stability of a drop on the top of a pillar was studied by determination of the free energy of the system depending on the apparent contact angle θ_{app} and the edge angle δ. The authors distinguished between four different cases for the drop stability. The first case describes a drop pinned on a sharp edge with a relatively small angle $40° \leq \delta \leq 60°$ (see Fig. 2.6 (a)). In this case, no movement of the contact line over the edge occurs despite of an increasing of the drop volume if $\delta \leq \theta_s$. The energy minimum of the system is reached when $\theta_{app} = 160°$. With increasing volume of the drop the most favorable position of the contact line is at the edge of the pillar. However, Chen et al. [20] mentioned a maximum volume for $\theta < \theta_{crit}$ beyond which a stable wall-edge-bound drop fails to exist. In Fig. 2.7, the maximum volume liquid drop on a solid edge with $\delta \leq \theta_s$ is illustrated by the solid black curve. The dot-dashed solid curve shows a liquid drop with a volume below the critical value, while the dotted curve refers to an unstable drop beyond the maximum curvature. In their work, the instability due to maximum curvature is related to drops on solid plates with zero thickness and finite width.

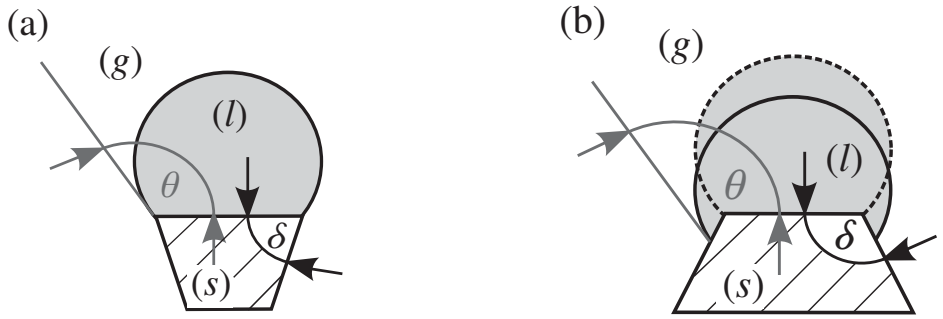

Figure 2.6: Drops on pillar. (a) shows an equilibrium configuration for $40° \leq \delta \leq 60°$, while (b) illustrates the initial drop configuration (dashed line) and the equilibrium configuration for $100° \leq \delta \leq 150°$ (solid line).

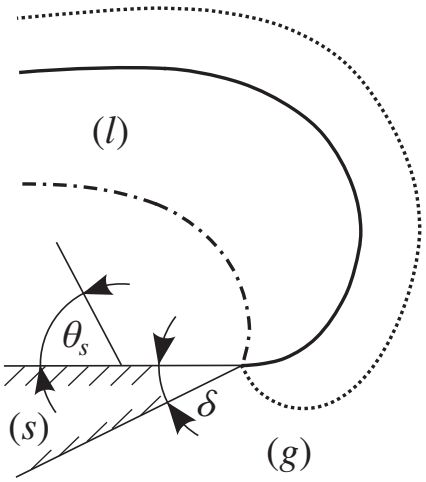

Figure 2.7: Cross section profiles of a liquid drop on a solid for $\delta \leq \theta_s$ according to Chen et al. [20]. The black solid curve refers to the maximum volume beyond which a stable curvature fails to exist.

Another case appears for $60° < \delta \leq 80°$ and a contact line which is initially pinned at the edge of the solid pillar [44]. For a critical value of θ_{app}, i.e., θ_{ls}, the contact line moves over the edge (compare Fig. 2.6 (b)). Further increase of the drop volume causes an increase of θ_{app} such that the contact line moves steadily over the edge. For $\theta_{app} \leq 160°$, the drop remains stable on the edge of the solid. However, the free energy in this case does not increase monotonically with increasing values of θ_{app}. Consequently, this system is regarded to be metastable, and the contact line will move over the edge of the solid with a slight increase of the energy, e.g., due to vibration of the pillar.

For $80° < \delta \leq 95°$, no drop can be suspended stable on the pillar. Fang and Amirfazli [44] mentioned the stability limit of a critical edge angle δ_{crit} according to Eq. 2.24 at which the drop collapses to the side walls of the pillar. To each value of δ in the range of 80° to 95°

corresponds a value of θ_{app}, at which the drop will split and will move down along the side walls immediately.

A last case is observed for $100° \leq \delta \leq 150°$: the free energy has a minimum value for all values of θ_{app}. The authors concluded that, for the contact line, it is not energetically favorable to stay on the edge of the pillar. However, after moving over the edge, the contact line will remain at a certain position at the wall (see Fig. 2.6 (b)).

2.4 Shape and Stability of Menisci on Solid Surfaces

Equilibrium surfaces in a cylindrical container with and without the influence of gravity have been studied widely. A general criterion for the existence and non-existence of a capillary surface either influenced or not by a longitudinal force was developed by Finn [45]. Chen and Collicott applied this criterion for symmetric [19] and asymmetric [21] cross-sections. The simplest case for capillary surfaces occurs when no body forces act on the system. For this case, one would assume that the shape of free surfaces in equilibrium in rotational symmetric containers would also be axisymmetric as it is mentioned e.g., by Dodge [37]. Concus and Finn showed first analytically [31] and later in experiments [32] that the profile is not necessarily axisymmetric as in exotic, rotational symmetric containers.

Padday [91, 92] analyzed axially symmetric meniscus profiles under the influence of gravity and classified these profiles into two types [91]. The bounded profiles cross the axis of symmetry and can be used to describe pendant or sessile drops (see Fig. 2.8). The unbounded type were labeled rod-in-free-surfaces, e.g., liquid bridges, and hole-in-the-liquid, e.g., annuli, respectively. A significant difference between these two profiles is that bounded menisci can be described by two (initial conditions), while unbounded meniscus profiles need three conditions for a complete definition, since the height of the profile has to be considered. Padday [91] also offered solutions for bounded menisci influenced by gravity: distorted nodaries to describe the shape of sessile drops and distorted undularies to characterize the profiles of pendant drops.

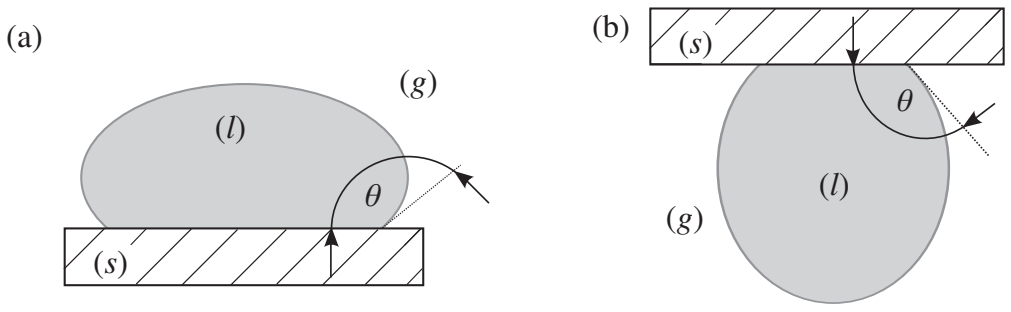

Figure 2.8: Bounded meniscus profiles: (a) sessile drop and (b) pendant drop.